**Atmospheric
Chemistry
and Physics
Discussions**

The spring 2011 final stratospheric warming above Eureka: anomalous dynamics and chemistry

C. Adams[1], K. Strong[1], X. Zhao[1], A. E. Bourassa[2], W. H. Daffer[3], D. Degenstein[2], J. R. Drummond[1,4], E. E. Farahani[1], A. Fraser[1,*], N. D. Lloyd[2], G. L. Manney[3,**,5], C. A. McLinden[6], M. Rex[7], C. Roth[2], S. E. Strahan[8], K. A. Walker[1,9], and I. Wohltmann[7]

[1]Department of Physics, University of Toronto, Toronto, Canada
[2]University of Saskatchewan, Saskatoon, Saskatchewan, Canada
[3]Jet Propulsion Laboratory, California Institute of Technology, Pasadena, USA
[4]Department of Physics and Atmospheric Sciences, Dalhousie University, Halifax, Canada
[5]New Mexico Institute of Mining and Technology, Socorro, New Mexico, USA
[6]Environment Canada, Downsview, Ontario, Canada
[7]Alfred Wegener Institute for Polar and Marine Research, Potsdam, Germany
[8]Universities Space Research Association, Columbia, Maryland, USA
[9]Department of Chemistry, University of Waterloo, Waterloo, Canada
[*]now at: School of GeoSciences, University of Edinburgh, Edinburgh, UK
[**]now at: NorthWest Research Associates, Socorro, New Mexico, USA

Title Page

Abstract	Introduction
Conclusions	References
Tables	Figures

|◄ | ►|

◄ | ►

Back | Close

Full Screen / Esc

Printer-friendly Version

Interactive Discussion

The spring 2011 final stratospheric warming above Eureka

C. Adams et al.

Full Screen / Esc

Abstract

In spring 2011, the Arctic polar vortex was stronger than in any other year on record. As the polar vortex started to break up in April, ozone and NO_2 columns were measured with UV-visible spectrometers above the Polar Environment Atmospheric Research Laboratory (PEARL) in Eureka, Canada (80.05° N, 86.42° W) using the differential optical absorption spectroscopy (DOAS) technique. These ground-based column measurements were complemented by Ozone Monitoring Instrument (OMI) and Optical Spectrograph and Infra-Red Imager System (OSIRIS) satellite measurements, Global Modeling Initiative (GMI) simulations, and dynamical parameters. On 8 April 2011, NO_2 columns above PEARL from the DOAS, OMI, and GMI datasets were approximately twice as large as in previous years. On this day, temperatures and ozone volume mixing ratios above Eureka were high, suggesting enhanced chemical production of NO_2 from NO. Additionally, GMI NO_x and N_2O fields suggest that downward transport along the vortex edge and horizontal transport from lower latitudes also contributed to the enhanced NO_2. The anticyclone that transported lower-latitude NO_x above PEARL became frozen-in and persisted in dynamical and GMI N_2O fields until the end of the measurement period on 31 May 2011. Ozone isolated within this frozen-in anticyclone (FrIAC) in the middle stratosphere was depleted due to reactions with the enhanced NO_x. Ozone loss was calculated using the passive tracer technique, with passive ozone profiles from the Lagrangian Chemistry and Transport Model, ATLAS. At 600 K, ozone losses between 1 December 2010 and 20 May 2011 reached 4.2 parts per million by volume (ppmv) (58 %) and 4.4 ppmv (61 %), when calculated using GMI and OSIRIS ozone profiles, respectively. This middle-stratosphere gas-phase ozone loss led to a more rapid decrease in ozone column amounts in April/May 2011 compared with previous years. Ground-based, OMI, and GMI ozone total columns within the FrIAC all decreased by more than 100 DU from 15 April to 20 May. Two lows in the ozone columns were also investigated and were attributed to a vortex remnant passing above Eureka at ∼ 500 K on 12/13 May and an ozone mini-hole on 22/23 May.

1 Introduction

During the spring-time break-up of the Arctic polar vortex, large variability in stratospheric trace gases can be observed as vortex and lower-latitude air masses mix. Fragments of the polar vortex, containing characteristic values of chemical tracers, such as low N_2O, can become "frozen-in" and be advected throughout the hemisphere (e.g., Hess, 1991). Similarly, lower-latitude air masses, containing, e.g., enhanced N_2O, can be transported northward. In some cases, these low-latitude air masses remain intact through the summer. These so-called frozen-in anticyclones (FrIACs) were observed in 2003 (Lahoz et al., 2007), 2005 (Manney et al., 2006; Allen et al., 2011), and 2007 (Thieblemont et al., 2011). The 2005 FrIAC formed during the final stratospheric warming and persisted until late May in dynamical fields, and until late summer in chemical tracer fields measured by the Microwave Limb Sounder (MLS) satellite instrument (Manney et al., 2006). These features were also captured by the Global Modeling Initiative (GMI) chemistry transport model (CTM) (Allen et al., 2011).

Ozone volume mixing ratios (VMRs) within frozen-in features depend primarily on middle stratosphere chemistry, as the air masses are isolated. Photochemical production through odd-oxygen reactions depends primarily on solar zenith angle (SZA), while catalytic loss depends primarily on NO_x concentrations and SZA. For large SZA (limited sunlight), both the photochemical production and catalytic destruction of ozone are slow. However, production drops off more rapidly with SZA than does destruction. This leads to a maximum ozone loss rate for SZA 80–95° (Sinnhuber et al., 1999).

In the winter, low-ozone pockets have been observed inside anticyclones shortly after the peak of a stratospheric warming (Manney et al., 1995a; Harvey et al., 2002, 2004, 2008). Low-ozone pockets form because the anticyclone isolates the air mass from ozone-rich lower-latitude air and sunlight is limited, repressing the photochemical production of ozone (Morris et al., 1998; Nair et al., 1998). Low-ozone pockets tend to have 5–30 % less ozone than surrounding ambient air (Harvey et al., 2008). In the summer, lower ozone has also been noted inside anticyclones, but is typically attributed

to dynamics instead of chemistry (Orsolini et al., 2003; Orsolini and Nikulin, 2006). Overall, summertime ozone loss is driven by 24-h sunlight, as NO_x is released from its night-time reservoirs, leading to a $\sim 30\%$ decrease in the ozone column (e.g., Farman et al., 1985; Perliski et al., 1989; Fahey and Ravishankara, 1999).

⁵ Spring-time polar ozone loss is typically associated with heterogeneous chemistry in the lower stratosphere. However, Konopka et al. (2007) found that NO_x-driven middle stratosphere ozone loss during stratospheric warmings can have a greater impact than halogens for some Arctic springs. They studied the transport of subtropical ozone and NO_x-rich air to the Arctic in spring 2003, a year in which the Arctic lower stratosphere

¹⁰ was warm. By late April 2003, local ozone loss was up to 50% at the 600-K potential temperature level and was dominated by NO_x chemistry, which accounted for 76% of the loss for the region between 600 and 900 K. Therefore, the ozone loss rates were strongly dependent on the amount of NO_y transported from lower latitudes.

In spring 2011, the Arctic polar vortex was stronger through February and March

¹⁵ than in any other year on record (Manney et al., 2011). Because of persistently low temperatures, continuous depletion via heterogeneous chemistry was observed until 20 April, leading to record ozone loss (Balis et al., 2011; Manney et al., 2011). These findings have been investigated with differential optical absorption spectroscopy (DOAS), Fourier transform infrared spectrometer, radiosonde, and lidar measurements

²⁰ taken at the Polar Environment Atmospheric Research Laboratory (PEARL) in Eureka, Canada (80.05° N, 86.42° W) by the Canadian Network for the Detection of Atmospheric Change (CANDAC) (Adams et al., 2012b; Lindenmaier et al., 2012).

In early April 2011, DOAS NO_2 columns above PEARL reached approximately twice the column amount observed during the same season in previous years (Adams et al.,

²⁵ 2012b). Therefore, we present an investigation of ground-based, satellite, and model NO_2 and ozone data above PEARL in April/May 2011. N_2O and aerosol are used as dynamical tracers, with low N_2O and aerosol indicating vortex air masses and high N_2O and aerosol indicating lower-latitude air masses (e.g., Ruth et al., 1994; Harvey et al., 1999). The ground-based, satellite, and model datasets used in this study are

described in Sect. 2. The evolution of these datasets above Eureka in the context of previous years is presented in Sect. 3.1. The relative roles of chemistry and transport in the large increase in the NO_2 column are discussed in Sect. 3.2. The subsequent development and evolution of a FrIAC, and middle-stratosphere gas-phase ozone loss is investigated in Sect. 3.3. In Sect. 3.4 and Sect. 3.5, a vortex fragment and an ozone mini-hole over Eureka are illustrated. Conclusions are given in Sect. 4.

2 Datasets

For this study, ground-based, satellite, and model datasets were combined in order to produce a complete picture of the vortex break-up in 2011 above Eureka. Ground-based DOAS measurements were used to identify unusual variations in ozone and NO_2 columns above Eureka. Ozone and NO_2 profiles were then resolved using Optical Spectrograph and Infra-Red Imager System (OSIRIS) satellite measurements. OSIRIS aerosol measurements were also used to identify vortex and lower-latitude air masses. Ozone Monitoring Instrument (OMI) satellite ozone and NO_2 column measurements complemented these datasets, in particular in early April, when OSIRIS was turned off for annual maintenance. The evolution of ozone and NO_2 was investigated using meteorological fields from Derived Meteorological Products (DMPs) and modeled ozone, NO_2, and N_2O from the GMI CTM. Since passive ozone was not available from the GMI runs used in this study, ATLAS passive ozone was used to quantify NO_x-driven ozone loss during these events. These datasets are described in the sections below.

2.1 DOAS ozone and NO_2

Ozone and NO_2 columns were measured above PEARL by two UV-visible DOAS instruments: the PEARL and University of Toronto ground-based spectrometers (GBSs) (Fraser et al., 2009). Measurements were taken at PEARL (prior to 2005, the Arctic Stratospheric Ozone Observatory – AStrO), which has been operated by CAN-

DAC since 2005. Measurements included in this study were acquired during CANDAC routine operations (August 2006 to present) and the Canadian Arctic ACE Validation Campaigns (springs 2004–2011) (Kerzenmacher et al., 2005; Fraser et al., 2008). The GBSs are part of the Network for the Detection of Atmospheric Composition Change (NDACC) and their Eureka ozone and NO_2 datasets are described in detail by Adams et al. (2012a). Measurements from the two GBS instruments are nearly identical and therefore were combined into a single GBS dataset.

The GBSs are UV-visible Triax-180 triple-grating spectrometers, built by Instruments S.A./Jobin Yvon Horiba, with cooled charge-coupled device detectors and a 2° field-of-view. The resolution of the GBSs varies from 0.2–2.5 nm depending on the selected grating and wavelength range. The GBSs recorded spectra in April and/or May at Eureka in 1999, 2003, 2004 and 2007–2011. Only data from 2004–2011 are used in the present study for consistency with GMI and OMI.

Ozone and NO_2 differential slant column densities (DSCDs) were retrieved using the DOAS technique with the QDOAS software (Fayt et al., 2011). Ozone DSCDs were analyzed using the NDACC recommendations published in Hendrick et al. (2011) in the 450–545 nm and 450–540 nm fitting windows for the UT-GBS and PEARL-GBS, respectively. The following cross-sections were all fit during the DOAS procedure: ozone measured at 223 K (Bogumil et al., 2003), NO_2 measured at 220 K (Vandaele et al., 1998), H_2O (converted from line parameters given in Rothman et al., 2003), wavelength-corrected O_4 (Greenblatt et al., 1990), and the Ring pseudoabsorber (Chance and Spurr, 1997), which accounts for the filling in of absorption lines due to Raman scattering. An additional cross-section was applied to correct for systematic polarization errors in the analysis. NO_2 was retrieved in two different wavelength regions: 425–450 nm (GBS-vis) and 350–380 nm (GBS-UV), depending on the selected grating. The NO_2-vis DSCDs were retrieved using the same cross-sections as ozone, with the addition of a first-order offset correction to account for stray light. Polarization correction cross-sections were not necessary for NO_2, perhaps due to the shorter wavelength region of the analysis. For NO_2-UV, a BrO cross-section measured

Discussion Paper | Discussion Paper | Discussion Paper | Discussion Paper

Title Page

Abstract | Introduction

Conclusions | References

Tables | Figures

◄ | ►

◄ | ►

Back | Close

Full Screen / Esc

Printer-friendly Version

Interactive Discussion

at 223 K (Fleischmann et al., 2004) and an OClO cross-section measured at 204 K (Wahner et al., 1987) were also included in the analysis.

Ozone and NO_2 vertical columns were retrieved from DSCDs using the Langley method in the SZA 86–91° range, or the nearest available SZA, with air mass factor look-up tables provided by the Belgian Institute for Space Aeronomy (IASB-BIRA). The ozone air mass factors produce total columns (Hendrick et al., 2011), while the NO_2 air mass factors produce partial columns from 17 km to the top of the atmosphere (Appendix A of Adams et al., 2012a). On average, errors of 6.0 % for ozone, 19 % for NO_2-vis and 19 % for NO_2-UV were calculated for April/May GBS measurements. The mean relative differences between OSIRIS and GBS columns in the Arctic are 5.7 % for ozone, −7.3 % for GBS-vis NO_2, and −3.3 % for GBS-UV (Adams et al., 2012a).

2.2 OSIRIS ozone, NO_2, and aerosol

OSIRIS was launched aboard the Odin spacecraft in February 2001 (Murtagh et al., 2002; Llewellyn et al., 2004). It observes limb-radiance profiles with a 1-km vertical field-of-view over altitudes ranging from approximately 10–100 km, with coverage from 82.2° N to 82.2° S. The grating Optical Spectrograph measures scattered sunlight from 280–800 nm, with 1-nm spectral resolution. The OSIRIS 25-km tangent height is within 500 km of Eureka $\sim$ 5–10 times per day and measurements of ozone, aerosol, and NO_2 are taken during the sunlit part of the year (from approximately 1 March to 15 October above Eureka).

The SaskMART Multiplicative Algebraic Reconstruction Technique (Degenstein et al., 2009) v5.0x (v5.0.1 and v5.0.6) ozone and aerosol were used in this study. Ozone absorption information in both the UV and visible parts of the spectrum is used to retrieve number density profiles from 60 km to the cloud tops (down to a minimum of 10 km in the absence of clouds). OSIRIS ozone VMRs, calculated using European Centre for Medium-Range Weather Forecasts (ECMWF) number density and neutral density profiles, are also available. SaskMART v5.0x ozone profiles agree with those from SAGE II (Stratospheric Aerosol and Gas Experiment) to within 2 % from 18–53 km

(Degenstein et al., 2009). Systematic and other errors are expected to be on the same order as the instrument noise. SaskMART aerosol extinction at 750 nm (Bourassa et al., 2007) is retrieved with an assumed height profile and a single-mode log-normal particle size distribution. OSIRIS aerosol agrees with SAGE II and SAGE III measurements to within 15 % for the lower stratosphere (Bourassa et al., 2012).

For NO_2, the v3.0 Optimal Estimation data product was used. NO_2 slant column densities (SCDs) are retrieved using the DOAS technique in the 435–451 nm range. These SCDs are converted to number density profiles from 10–46 km using an optimal estimation inversion, with high response for 15–42 km (Brohede et al., 2008). OSIRIS NO_2 VMRs, calculated from ECMWF number density and neutral density profiles, are also available. The precision of these measurements is 16 % between 15–25 km and 6 % between 25–35 km based on comparisons with other instruments (OSIRIS, 2011).

To investigate air masses above Eureka, OSIRIS ozone, aerosol, and NO_2 profiles were averaged daily within 500 km of Eureka. To produce polar maps at fixed potential temperature levels, data were passed through a Gaussian filter with a 5° standard deviation onto a $5 \times 5°$ grid. For each grid-point, the angular distance between the grid-point and the OSIRIS measurements was calculated. Weights based on the angular distance between the measurements and the grid-point were calculated using a Gaussian function, with a standard deviation of 5°. The weighted mean of OSIRIS measurements at the given grid-point was then calculated. If the sum of weights at a given grid-point was < 1, the grid-point was left empty. The filter and interpolation grid were tested for various cases to ensure that smoothing and interpolation were not introducing any spurious features to the maps. The 5° filter provided the best balance between showing the detail in the OSIRIS measurements, without introducing large gaps in the figure. The choice of interpolation grid did not have a significant impact on the maps for the measurement dates considered.

C. Adams et al.

Title Page

Abstract | Introduction

Conclusions | References

Tables | Figures

⏮ | ⏭

◀ | ▶

Back | Close

Full Screen / Esc

Printer-friendly Version

Interactive Discussion

2.3 OMI ozone and NO$_2$

OMI (Levelt et al., 2006), on board the Earth Observing System Aura satellite, measures sunlight backscattered from the Earth's surface at UV and visible wavelengths. OMI takes measurements in the sunlit part of the globe, with a nadir resolution that varies from $13 \times 24\,km^2$ to $24 \times 48\,km^2$ and daily global coverage.

OMIDOAO3 ozone total columns are retrieved using an algorithm that is based on the DOAS technique (Veefkind et al., 2006; Veefkind and Sneep, 2009). Fits are performed in a 5-nm-wide fitting window, centred at 334.1 nm. AMFs are determined using a radiative transfer model. OMDOAO3 total columns have been validated extensively against other instruments and have been shown to agree typically within 2 % or better, with a slight SZA dependence at high latitudes (e.g., McPeters et al., 2008 and references therein). Hendrick et al. (2011) found that OMIDOAO3 columns agreed with high-latitude ground-based DOAS measurements to within $\sim 5\,\%$.

The Dutch OMI NO$_2$ retrieval (DOMINO) stratospheric NO$_2$ product was used in this study (Boersma et al., 2007; Boersma et al., 2011; Dirksen et al., 2011). NO$_2$ SCDs are retrieved using the DOAS technique in the 405–465 nm range. SCDs are then assimilated in a CTM and stratospheric partial columns are produced. DOMINO stratospheric NO$_2$ agrees with ground-based measurements to within $0.3 \times 10^{15}\ mol\,cm^{-2}$ (13 %) (Dirksen et al., 2011).

To investigate air masses above Eureka, daily OMI ozone and NO$_2$ columns within 500 km of Eureka were averaged. To produce polar maps at fixed potential temperature levels, data were passed through a Gaussian filter with a standard deviation of 1° and interpolated onto $1° \times 1°$ horizontal grid, using the method described in Sect. 2.2. Note that a smaller grid and standard deviation were used for OMI than for OSIRIS because OMI has better horizontal resolution.

2.4 DMPs

DMPs (Manney et al., 2007) were calculated daily at 12:00 UTC directly above PEARL using the GEOS Version 5.1.0 and 5.2.0 (GEOS-5) analyses (Reinecker, 2008). DMP temperatures, scaled potential vorticity (sPV, potential vorticity scaled in "vorticity units"
5 to give a similar range of values at each level, e.g., Dunkerton and Delisi, 1986; Manney et al., 1994) and equivalent latitude (EqL, the latitude that would enclose the same area as a given PV contour, e.g., Butchart and Remsberg, 1986) were all considered in this study. sPV values of $1.6 \times 10^{-4} \, \text{s}^{-1}$ and $1.2 \times 10^{-4} \, \text{s}^{-1}$ are used to define the inner and outer vortex edges, respectively (Manney et al., 2007). Manney et al (2007)
10 and Lindenmaier et al (2012) have shown that using a single sPV value to define the vortex edge throughout the fall/winter/spring season gives comparable results to other commonly used vortex edge identification methods. EqL provides a coordinate system that separates air masses inside and outside the polar vortex.

2.5 GMI

15 GMI is a 3-D CTM (Strahan et al., 2007) with full chemistry in the troposphere and stratosphere (Duncan et al., 2007). The GMI CTM is integrated with meteorological fields from the GEOS-5.2.0 Modern Era Retrospective-analysis for Research and Applications (MERRA) (Rienecker et al., 2011). The GMI chemical formulation includes 125 species, with 322 thermal chemical reactions, 82 photolysis reactions, including
20 heterogeneous reactions on aerosols and polar stratospheric clouds. Time-varying natural and anthropogenic emissions are included. Tropospheric processes represented in the simulation include convection, wet scavenging, dry deposition, and NO_x produced from lightning (Allen et al., 2010). The GMI-MERRA simulation is integrated at $2° \times 2.5°$ (latitude × longitude) on 72 pressure levels, ranging from the surface to 0.015 hPa. For
25 this study, daily ozone, NO_2, and NO fields used are averaged for 10:00–11:00 LT, in order to sample NO and NO_2 at the same part of the diurnal cycle throughout the Northern Hemisphere (e.g., at a fixed LT). N_2O was not available in the GMI 10:00–11:00 LT

model output. Therefore, N_2O, PV, and temperature are model "snapshots" from the daily 12:00 UTC model output. Profiles were interpolated to the latitude and longitude of Eureka. Polar maps at various potential temperature levels were also produced.

2.6 ATLAS passive ozone

Passive ozone was calculated using the Lagrangian Chemistry and Transport Model ATLAS (Wohltmann and Rex, 2009; Wohltmann et al., 2010). Ozone was treated as a passive dynamical tracer with no chemistry. The passive tracer was initialized on 1 December 2010, using profiles from MLS. Meteorological data from the ECMWF ERA-Interim reanalysis are used to drive the model (Dee et al., 2011). The model resolution is approximately 150 km in the horizontal and 1–2 km in the vertical. The model uses a hybrid vertical coordinate, which is to a good approximation a potential temperature coordinate. Heating rates from the ERA-Interim reanalysis drive the vertical motion. Transport and mixing in ATLAS passive ozone has been validated against other models and datasets and was found to be in good agreement (Wohltmann and Rex, 2009).

3 Results

3.1 The springtime stratosphere above Eureka in 2011

Figure 1 shows the timeseries of NO_2 and ozone columns above Eureka from GBS ground-based measurements (top), OMI satellite overpasses (middle), and GMI model output (bottom). The 2004–2010 data is shown in grey and the 2011 data in red. Good agreement is observed between the three datasets. In years prior to 2011, NO_2 columns increase during April and May as hours of sunlight at Eureka increase (SZAs decrease). This is expected as NO_x is released from night-time reservoirs through photochemical reactions. Note that only qualitative agreement is expected, as the seasonal increase in NO_2 depends on the SZA at which NO_2 is sampled. Ozone columns decrease throughout the spring, as descent in the polar vortex ceases. In 2011, NO_2 and

ozone columns are low on 4 April, when the polar vortex briefly passes above Eureka. On 8 April (labeled A), NO_2 increases to values that are nearly two times larger than in previous years in all three datasets. This is attributed to NO_x transport and the chemical production of NO_2 in Sect. 3.2. Throughout the rest of April/May, NO_2 columns
5 gradually return to values that are comparable to previous years. Ozone total columns also increase in early April, reaching maxima between $\sim$ 10–15 April. They then decrease throughout the rest of April/May, at a faster rate than in previous years, due to enhanced heterogeneous NO_x chemistry within a FrIAC, as discussed in Sect. 3.3. Ozone columns above Eureka also decrease on 12/13 May (labeled B) due to a vortex
10 fragment at 500 K, described in Sect. 3.4, and on the 22/23 May (labeled C) due to an ozone mini-hole, as shown in Sect. 3.5.

Profiles of dynamical parameters, trace gases, and aerosol extinction are shown in Fig. 2 for 2011 (red lines) and 2004–2010 (grey lines). Average profiles for 2011 (blue dashed lines) and 2004–2010 (thick black lines) are also shown. Note that approximate
15 altitudes corresponding to the potential temperature levels are given on the right y-axis of panel a. Temperatures above Eureka (panel a) in 2011 reached the highest values in the record from 400 to 1000 K. Average April/May 2011 temperatures are also higher than average temperatures in previous years for 400–1400 K. EqLs (panel b) in 2011 are smaller than observed in all of the previous years ($<$ 30° N between 700 K and
20 1400 K, and at $\sim$ 450 K) suggesting the transport of lower-latitude air above Eureka. Therefore, the warm temperatures are likely due to the poleward advection of warm tropical air over Eureka. OSIRIS NO_2 VMRs (panel c) are enhanced in 2011 for 500–1400 K, which is consistent with the large NO_2 column amounts (Fig 1a,c,e). OSIRIS ozone VMRs (panel d) in 2011 are on average smaller than in previous years for po-
25 tential temperature levels below 1300 K. OSIRIS aerosol extinction (panel e) and GMI N_2O VMRs (panel f) are larger in 2011 than previous years above $\sim$ 650 K, suggesting enhanced transport of lower-latitude air over Eureka. Average GMI NO_x ($NO + NO_2$) (panel i) is larger in 2011 than previous years for potential temperature levels $>$ 500 K.

The spring 2011 final stratospheric warming above Eureka

C. Adams et al.

Title Page

Abstract	Introduction
Conclusions	References
Tables	Figures

|◄ | ►|

◄ | ►

Back | Close

Full Screen / Esc

Printer-friendly Version

Interactive Discussion

For potential temperature levels $> 700\,\text{K}$, many of the April/May 2011 NO_x profiles are larger than in any other year.

Figure 3 shows the evolution of temperature (panel a) and EqL (panel b) above Eureka during April and May of 2011. The white contour lines indicate $sPV = 1.6 \times 10^{-4}\,\text{s}^{-1}$, which can be used to approximate the inner vortex edge. Air masses within these contour lines are considered to be inside the polar vortex. Select N_2O contours (black) are overlaid above the EqL. On 4 April, the vortex is above Eureka from 550 to 1450 K. Above 600 K, the vortex is displaced from Eureka on 5 April. Between 4 and 6 April, temperatures rise rapidly (from 226 to 246 K at the 850-K potential temperature level) and EqL decreases sharply (from 81° to 40° at the 850-K potential temperature level). This suggests that the high temperatures are due to the rapid poleward transport of lower-latitude air. Low EqL (values $< 30°$) and enhanced N_2O indicate tropical air for ~ 10–20 April between ~ 700–1100 K. The altitude range of low EqL narrows with time, remaining $< 30°$ only at $\sim 600\,\text{K}$ by the end of May. During May, as SZAs decrease and more sunlight enters the atmosphere, temperatures gradually increase. At altitudes below 600 K, the vortex gradually moves away from Eureka until 13 April. Following ~ 20 April, there are intervals of high and low EqL (coinciding with low and high N_2O), suggesting that vortex and lower-latitude air are moving above Eureka.

GMI NO_2, with NO_x contours overlaid (black lines) (panel c) and GMI ozone (panel d) are also shown in Fig. 3. Note that GMI data is shown because OSIRIS did not take measurements in early April. During the period of overlap, good agreement between OSIRIS and GMI was observed. As the vortex moves away from Eureka, NO_2 VMRs increase and correspond to high temperatures (panel a) and large ozone VMRs (panel d). The enhanced NO_2 VMRs are further investigated in Sect. 3.2. Reduced ozone VMRs approximately follow low EqLs (panel b) as they descend in altitude from 15 April to 31 May. This is discussed further in Sect. 3.3.

3.2 NO_2 maximum on 8 April

A large maximum was observed in the NO_2 column (Fig. 1a, c, e, event A) and profile timeseries (Fig. 2c) on 8 April 2011. The chemical production of NO_2 from NO_x is favoured for high temperatures and large ozone VMRs (e.g., Sander et al., 2011). Above Eureka, enhanced NO_2 on 8 April corresponds to large ozone VMRs and high temperatures for potential temperature levels > 600 K (Fig. 3), suggesting the chemical production of NO_2 from NO. Additionally, NO_x increases as the vortex moves away, suggesting that transport also plays a role (Fig. 3c, black contours). This section describes the synoptic evolution of the transport and chemical production of NO_2 from 1–8 April.

Figure 4 shows polar maps of OMI ozone total columns and NO_2 stratospheric partial columns for 1, 3, 5, and 8 April 2011. $sPV = 1.6 \times 10^{-4}\,s^{-1}$ contours, which approximately enclose the polar vortex, are also shown for three potential temperature levels. On 1 April, low ozone and NO_2 columns reside over Siberia and Northern Europe, coinciding with the location of the polar vortex. On 3 and 5 April, low ozone and NO_2 columns stretch toward Eureka as the polar vortex shifts and stretches overhead. By 8 April, the low NO_2 columns have stretched into a "C" shape, with Eureka and very high NO_2 columns at its centre. The low in ozone remains across the pole from Eureka. Low NO_2 columns coincide approximately with the location of the polar vortex in the middle stratosphere (~ 850 K), while low ozone columns coincide with the lower stratosphere vortex (~ 500 K). This is consistent with the differences between the altitudes of the ozone and NO_2 number density maxima.

Polar maps of GMI NO_2, ozone, N_2O, and NO_x for 1, 3, 5, and 8 April at 600 K (~ 23 km) are shown in Fig. 5. This is the altitude of the NO_2 number density maximum above Eureka in 2011 according to OSIRIS profiles and therefore yields the largest contribution to the NO_2 columns. The polar vortex (bounded by the white PV contours), encloses low NO_2, ozone, N_2O, and NO_x. At this level, the vortex moves over Eureka on 5 April as a pocket of warm air (enclosed by the purple contour line) appears between

Title Page

Abstract | Introduction

Conclusions | References

Tables | Figures

|◄ | ►|

◄ | ►

Back | Close

Full Screen / Esc

Printer-friendly Version

Interactive Discussion

Alaska and Siberia. On 8 April, the pocket of warm air is situated directly above Eureka, the vortex has stretched away and NO_2 is enhanced. The NO_2/NO_x ratio above Eureka is 2.4–4.4 times larger than in previous years on the same date. NO_x VMRs above Eureka on 8 April 2011 are comparable to previous years, but they are 1.5–2 times larger than surrounding air masses (Fig. 5p). North of Eureka, NO_x-rich air is located along the vortex edge, where N_2O is low, suggesting the downward transport of higher-altitude NO_x-rich and N_2O-poor air. Transport of lower-latitude air, indicated by high N_2O, is located southwest of Eureka. This suggests that the NO_x-rich air that has been transported downward along the vortex edge was drawn over Eureka between the polar vortex to the north and lower-latitude air to the south. Therefore, the high NO_2 VMRs above Eureka are due to both downward transport and chemical production at 600 K.

Figure 6 shows polar maps of GMI NO_2, ozone, N_2O and NO_x at 850 K ($\sim$ 31 km), the altitude of the large increase in GMI NO_2 VMRs (Fig. 3d) and the altitude at which OMI NO_2 columns appear to follow the shape of the polar vortex (Fig. 4). Low-latitude air, indicated by high N_2O, is transported from Northern Europe, wrapping counter-clockwise around the vortex. By 8 April, the vortex has shifted to a "C" shape, with high temperatures and NO_2 at its center, directly above Eureka. At this altitude, the ratio of NO_2/NO_x above Eureka is 2.0–4.6 times larger in 2011 than on the same date in previous previous years. At this level, the NO_2 increase is dominated by production from NO, due to the high temperatures. Enhanced lower-latitude ozone is also transported poleward, and VMRs decrease as it reaches Eureka. This is discussed further in Sect. 3.3.

Above 1000 K, temperatures above Eureka are normal within the context of previous years, but NO_x and NO_2 are enhanced (Fig. 2a, c, g) and strong poleward transport of NO_x is apparent in synoptic maps (not shown here). Therefore, at these altitudes, horizontal transport of NO_x from lower latitudes also contributes to the enhanced NO_2 columns.

3.3 FrIAC and middle-stratosphere ozone loss

In early April, lower-latitude air was transported above Eureka into an anticyclone. The early evolution of this anticyclone is evident in the GMI fields at 850 K, shown in Fig. 6. Low-latitude air, identified by high N_2O enclosed by PV contours, wraps counter-clockwise around the polar vortex. By 8 April, the edge of this air mass is above Eureka. Ozone VMRs inside the air mass on 1 April are enhanced, as is consistent with the transport of ozone-rich lower-latitude air. However, as the anticyclone moves over Eureka, the ozone VMRs within it decrease, suggesting chemical ozone loss. This section presents evidence that this anticyclone became frozen-in until at least the end of May and that gas-phase ozone loss occurred within it. The anticyclone persists at 850 K in PV contours and high N_2O throughout April, as shown in Fig. 7. OSIRIS and GMI ozone agree well, both showing filaments of high-ozone lower-latitude air being drawn around the anticyclone, and low ozone within the anticyclone. The anticyclone at 850 K remains centred above Eureka for 13–20 April and is then advected by easterly winds and begins to rotate around the pole, with the edge of the anticyclone remaining above Eureka.

This feature persists until at least the end of May, suggesting a 2011 FrIAC as is evident in Fig. 3b. EqLs (color scale) are low and N_2O VMRs (black contours) are enhanced until ~ 20 April as the anticyclone remains above Eureka. Following the advection of the anticyclone, N_2O maxima (and EqL minima) pass over Eureka on 1, 6, 21, and 29 May. Therefore the FrIAC has remained intact until at least the end of May in both tracer and dynamical fields. Low ozone VMRs (Fig. 3c) are first observed at ~ 1400 K on 6 April and gradually descend and are centered at ~ 1150 K on 12 April, ~ 850 K on 22 April, and ~ 700 K on 7 May. As the low ozone VMRs reach altitudes at which ozone number densities are larger, the total ozone columns above Eureka decrease (Fig. 1b, d, f). The low ozone VMRs coincide with the descent and periodicity of the FrIAC, suggesting that heteogeneous ozone loss occurs within the FrIAC. SZAs above PEARL range from ~ 75–95° on 1 April to ~ 60–80° on 31 May and are

therefore frequently within the 80–95° SZA range for which catalytic ozone destruction cycles (dominated by NO_x) lead to maximum ozone loss (Sinnhuber et al., 1999). Furthermore, NO_x was enhanced in 2011 compared with previous years (Fig. 2g).

Ozone loss above Eureka was estimated using the passive tracer technique (Manney et al., 1995b; WMO, 2003; e.g., Konopka et al., 2007) with ATLAS passive ozone, which was initialized on 1 December 2010 with MLS ozone data. Figure 8a shows the 2011 timeseries of ozone VMRs at 600 K from ATLAS passive ozone, OSIRIS, and GMI. Good agreement is observed between OSIRIS and GMI. The low ozone VMRs in early April coincide with the vortex passing above Eureka.

The timeseries of ATLAS passive ozone minus OSIRIS and GMI ozone at 600 K is shown in Fig. 8b. Prior to 15 April, much of the variability in ozone loss can be attributed to transport, as the polar vortex passes briefly over Eureka and an anticyclone moves overhead (see Sect. 3.2). On 15 April 2010, an ozone loss of ∼ 2 parts per million by volume (ppmv) is calculated. This is likely due to NO_x cycles since 1 December 2010, as low EqL values (see Fig. 3b) suggest that the air mass at 600 K originates from lower latitudes. Around 12/13 May (labelled B) an isolated vortex air mass passes over Eureka (see Sect. 3.4). Therefore, the reduction in ozone loss during this period is likely due to transport. The maximum ozone loss at 600 K since 1 December 2010 is observed on 20 May 2011 at 4.4 ppmv (61 %) for GMI and 4.2 ppmv (58 %) for OSIRIS. Ozone losses of ∼ 3 ppmv between 1 December 2010 and 1 May 2011 are comparable to the losses observed by Konopka et al. (2007) at 600 K between 1 December 2002 and 1 May 2003. Konopka et al. (2007) attributed this ozone loss to transport of NO_x during several stratospheric warmings earlier in the year.

Ozone loss due to NO_x chemistry above Eureka was calculated between 1 April and 31 May for 2004–2011, using GMI monthly average O_x loss rates due to $NO_2 + O \rightarrow NO + O_2$. Note that these average loss rates include processes inside the polar vortex in early April and within the vortex fragment on 12/13 May, as well as within the FrIAC. NO_x-driven ozone loss above Eureka was larger in 2011 than in any previous year from the tropopause to 18 hPa (∼ 700 K) and above 6.9 hPa (∼ 1000 K). At 37 hPa

The spring 2011 final stratospheric warming above Eureka

C. Adams et al.

Title Page

Abstract	Introduction
Conclusions	References
Tables	Figures

⏮   ⏭

◀   ▶

Back   Close

Full Screen / Esc

Printer-friendly Version

Interactive Discussion

(~ 600 K), there was 1.2 ppmv of ozone loss due to NO_x chemistry above Eureka in 2011 compared with 0.7–0.9 ppmv in previous years. This is smaller than the apparent ~ 2 ppmv of ozone lost between between 1 April and 31 May 2011 above Eureka, calculated using ATLAS passive ozone and GMI and OSIRIS ozone VMRs (Fig. 8). This suggests that some of the ozone loss observed in the passive ozone timeseries occurred before the air mass reached Eureka. This is consistent with Fig. 6, which shows ozone VMRs decreasing as air masses are transported from lower latitudes toward Eureka.

3.4   Vortex fragment on 12/13 May

Ozone and NO_2 columns decreased on 12/13 May (Fig. 1, event B). These low columns coincided with high EqLs, low temperatures, and low ozone VMRs at ~ 500 K (Fig. 3). Figure 9 shows the evolution of this event at 500 K in OSIRIS ozone and aerosol and GMI ozone and N_2O. Good agreement is observed between GMI and OSIRIS ozone. The approximate outer vortex edge (sPV = 1.2×10^{-4} s^{-1}, dashed white lines) and inner vortex edge (sPV = 1.6×10^{-4} s^{-1}, thick white lines) are also indicated. Low ozone, N_2O, and aerosol are enclosed within the vortex across the pole from Eureka on 26 April. This air mass is stretched and a vortex remnant moves over Northern Europe in early May. On 13 May, the vortex remnant passes over Eureka, leading to the low ozone column measurements. This is consistent with other studies that have observed confined fragments of vortex air during and following the spring stratospheric final warming (e.g., Hess, 1991).

3.5   Ozone mini-hole on 22/23 May

Minimum ozone columns of 294 DU, 283 DU, and 311 DU are observed above Eureka in the GBS, OMI and GMI datasets around 22/23 May 2011 (Fig. 1b, d, e, event C). Figure 10 shows the evolution of this event. On 22 May, a large pocket of low ozone (< 300 DU) is observed in OMI total column data over the pole and Ellesmere Island

C. Adams et al.

Full Screen / Esc

Discussion Paper | Discussion Paper | Discussion Paper | Discussion Paper

(panel a). This coincides with low GMI ozone VMRs (panel c) and high GMI N_2O VMRs (panel d) at 400 K. Equivalent latitudes are $< 50°$ above Eureka (not shown here) for 350–700 K on 22 May. This suggests that ozone-poor lower-latitude air has been transported above Eureka. Geopotential heights at 400 K (white contours, panels c, d) indicate that the isentropes around the minihole region are raised. The tropopause (panel b) is also elevated. This suggests that more ozone-poor tropospheric air is contributing to the total column. This is consistent with the formation of an ozone mini-hole, which can lead to large decreases in the ozone column over a short time period (e.g., Peters et al., 1995; James, 1998; Hood et al., 2001; Iwao and Hirooka, 2006). Ozone miniholes are caused by dynamical processes (e.g., Hood et al., 2001), usually resulting from a combination of the transport of lower-latitude ozone-poor air masses and a rise in the tropopause, as shown on 22 May 2011 above Eureka.

4 Conclusions

The evolution of ozone and NO_2 was observed above Eureka (80.05° N, 86.42° W) during and after the final warming of the record-strong polar vortex in spring 2011. Good qualitative agreement was observed between ground-based DOAS, OMI and OSIRIS satellite, and GMI model ozone and NO_2 during this period.

As the vortex moved away from Eureka on 8 April 2011, NO_2 columns were nearly twice as large as in previous years during the same period. This coincided with high temperatures and large ozone VMRs, suggesting chemical production of NO_2. Furthermore, GMI NO_x and N_2O fields suggest that at 600 K, near the NO_2 maximum, NO_x descended from higher altitudes along the vortex edge and became trapped above Eureka between a lower-latitude air mass and the vortex. Above the NO_2 maximum, NO_x-rich air was transported over Eureka from mid-latitudes into an anticyclone. This anticyclone became frozen-in and persisted until the end of the measurement period on 31 May 2011.

Ozone was trapped within this FrIAC and depleted by the enhanced NO_x. GMI ozone loss due to NO_x above Eureka for 1 April to 31 May was larger in 2011 than for any other year in the dataset (2004–2010) for most of the stratosphere, including the region containing the bulk of the ozone column, from the tropopause to 18 hPa (~ 700 K). Therefore, ozone columns decreased more rapidly in April/May 2011 than in previous years. Chemical ozone loss between 1 December and 20 May 2011, calculated using ATLAS passive ozone, reached 4.4 ppmv (61 %) in GMI data and 4.2 ppmv (58 %) in OSIRIS data at 600 K above Eureka.

On 12/13 May, a vortex remnant at ~ 500 K passed over Eureka, leading to a reduction in the ozone columns. Low ozone columns were also observed on 22/23 May and were consistent with the formation of an ozone mini-hole due to horizontal transport of lower-latitude ozone-poor air and a rise in the tropopause height.

As halogen concentrations decrease and N_2O emissions increase, N_2O, as a precursor to stratospheric NO_x, is becoming a significant contributor to anthropogenic ozone loss (e.g., Ravishankara et al., 2009; WMO, 2011). Furthermore, dynamical variability in the Arctic stratosphere appears to be increasing, with warm winters getting warmer and cold winters getting colder: the four warmest and the two coldest winters since the 1970s have occurred within the last decade (e.g., Manney et al., 2011). Substantial transport of lower-latitude NO_x and subsequent middle stratospheric ozone loss via gas-phase chemistry was previously observed in spring 2003, following a warm winter that was perturbed by a minor stratospheric warming in December and a major warming in January (Konopka et al., 2007). In the present study, similar middle-stratospheric ozone losses were observed during the break-up of the record-strength vortex in April/May 2011, indicating that significant NO_x transport and subsequent ozone loss can also follow an unusually cold, dynamically quiescent winter.

References

Adams, C., Strong, K., Batchelor, R. L., Bernath, P. F., Brohede, S., Boone, C., Degenstein, D., Daffer, W. H., Drummond, J. R., Fogal, P. F., Farahani, E., Fayt, C., Fraser, A., Goutail, F., Hendrick, F., Kolonjari, F., Lindenmaier, R., Manney, G., McElroy, C. T., McLinden, C. A., Mendonca, J., Park, J.-H., Pavlovic, B., Pazmino, A., Roth, C., Savastiouk, V., Walker, K. A., Weaver, D., and Zhao, X.: Validation of ACE and OSIRIS ozone and NO_2 measurements using ground-based instruments at 80° N, Atmos. Meas. Tech., 5, 927–953, doi:10.5194/amt-5-927-2012, 2012a.

The spring 2011 final stratospheric warming above Eureka

C. Adams et al.

Title Page

Abstract	Introduction
Conclusions	References
Tables	Figures

◄◄   ►►

◄   ►

Back   Close

Full Screen / Esc

Printer-friendly Version

Interactive Discussion

Adams, C., Strong, K., Zhao, X., Bassford, M. R., Chipperfield, M. P., Daffer, W., Drummond, J. R., Farahani, E. E., Feng, W., Fraser, A., Goutail, F., Manney, G., McLinden, C. A., Pazmino, A., Rex, M., and Walker, K. A.: Severe 2011 ozone depletion assessed with 11 years of ozone, NO_2, and $OClO$ measurements at 80° N, Geophys. Res. Lett., 39, L05806, doi:10.1029/2011GL050478, 2012b.

Allen, D., Pickering, K., Duncan, B., and Damon, M.: Impact of lightning NO emissions on North American photochemistry as determined using the Global Modeling Initiative (GMI) model, J. Geophys. Res., 115, D22301, doi:10.1029/2010JD014062, 2010.

Allen, D. R., Douglass, A. R., Manney, G. L., Strahan, S. E., Krosschell, J. C., Trueblood, J. V., Nielsen, J. E., Pawson, S., and Zhu, Z.: Modeling the Frozen-In Anticyclone in the 2005 Arctic Summer Stratosphere, Atmos. Chem. Phys., 11, 4557–4576, doi:10.5194/acp-11-4557-2011, 2011.

Balis, D., Isaksen, I. S. A., Zerefos, C., Zyrichidou, I., Eleftheratos, K., Tourpali, K., Bojkov, R., Rognerud, B., Stordal, F., Sovde, O. A., and Orsolini, Y.: Observed and modelled record ozone decline over the Arctic during winter/spring 2011, Geophys. Res. Lett., 38, L23801, doi:10.1029/2011GL049259, 2011.

Boersma, K. F., Eskes, H. J., Veefkind, J. P., Brinksma, E. J., van der A, R. J., Sneep, M., van den Oord, G. H. J., Levelt, P. F., Stammes, P., Gleason, J. F., and Bucsela, E. J.: Near-real time retrieval of tropospheric NO_2 from OMI, Atmos. Chem. Phys., 7, 2103–2118, doi:10.5194/acp-7-2103-2007, 2007.

Boersma, K. F., Braak, R., and Van Der A, R.: Dutch OMI NO_2 (DOMINO) data product v2.0: http://www.temis.nl/docs/OMI_NO2_HE5_2.0_2011.pdf (last access: 13 January 2012), 2011.

Bogumil, K., Orphal, J., Homann, T., Voigt, S., Spietz, P., Fleischmann, O. C., Vogel, A., Hartmann, M., Kromminga, H., Bovensmann, H., Frerick, J., and Burrows, J. P.: Measurements of molecular absorption spectra with the SCIAMACHY pre-flight model: instrument characterization and reference data for atmospheric remote-sensing in the 230–2380 nm region, J. Photoch. Photobio. A, 157, 167–184, doi:10.1016/S1010-6030(03)00062-5, 2003.

Bourassa, A. E., Degenstein, D. A., Gattinger, R. L., and Llewellyn, E. J.: Stratospheric aerosol retrieval with optical spectrograph and infrared imaging system limb scatter measurements, J. Geophys. Res., 112, D10217, doi:10.1029/2006JD008079, 2007.

Bourassa, A. E., Rieger, L. A., Lloyd, N. D., and Degenstein, D. A.: Odin-OSIRIS stratospheric aerosol data product and SAGE III intercomparison, Atmos. Chem. Phys., 12, 605–614, doi:10.5194/acp-12-605-2012, 2012.

Brohede, S., McLinden, C. A., Urban, J., Haley, C. S., Jonsson, A. I., and Murtagh, D.: Odin stratospheric proxy NO_y measurements and climatology, Atmos. Chem. Phys., 8, 5731–5754, doi:10.5194/acp-8-5731-2008, 2008.

Butchart, N. and Remsberg, E. E.: The Area of the Stratospheric Polar Vortex as a Diagnostic for Tracer Transport on an Isentropic Surface, J. Atmos. Sci., 43, 1319–1339, 1986.

Chance, K. V. and Spurr, R. J. D.: Ring effect studies: Rayleigh scattering, including molecular parameters for rotational Raman scattering, and the Fraunhofer spectrum, Appl. Opt., 36, 5224–5230, 1997.

Dee, D. P., Uppala, S. M., Simmons, A. J., Berrisford, P., Poli, P., Kobayashi, S., Andrae, U., Balmaseda, M. A., Balsamo, G., Bauer, P., Bechtold, P., Beljaars, A. C. M., van de Berg, L., Bidlot, J., Bormann, N., Delsol, C., Dragani, R., Fuentes, M., Geer, A. J., Haimberger, L., Healy, S. B., Hersbach, H., Holm, E. V., Isaksen, L., Kallberg, P., Koehler, M., Matricardi, M., McNally, A. P., Monge-Sanz, B. M., Morcrette, J. J., Park, B. K., Peubey, C., de Rosnay, P., Tavolato, C., Thepaut, J. N., and Vitart, F.: The ERA-Interim reanalysis: configuration and performance of the data assimilation system, Q. J. Roy. Meteor. Soc., 137, 553–597, 2011.

Degenstein, D. A., Bourassa, A. E., Roth, C. Z., and Llewellyn, E. J.: Limb scatter ozone retrieval from 10 to 60 km using a multiplicative algebraic reconstruction technique, Atmos. Chem. Phys., 9, 6521–6529, doi:10.5194/acp-9-6521-2009, 2009.

Dirksen, R. J., Boersma, K. F., Eskes, H. J., Ionov, D. V., Bucsela, E. J., Levelt, P. F., and Kelder, H. M.: Evaluation of stratospheric NO_2 retrieved from the Ozone Monitoring Instrument: Intercomparison, diurnal cycle, and trending, J. Geophys. Res., 116, D08305, doi:10.1029/2010JD014943, 2011.

Duncan, B. N., Strahan, S. E., Yoshida, Y., Steenrod, S. D., and Livesey, N.: Model study of the cross-tropopause transport of biomass burning pollution, Atmos. Chem. Phys., 7, 3713–3736, doi:10.5194/acp-7-3713-2007, 2007.

Dunkerton, T. J. and Delisi, D. P.: Evolution of Potential Vorticity in the Winter Stratosphere of January February 1979, J. Geophys. Res., 91, 1199–1208, 1986.

Fahey, D. W. and Ravishankara, A. R.: Summer in the stratosphere, Science, 285, 208–210, 1999.

Farman, J. C., Murgatroyd, R. J., Silnickas, A. M., and Thrush, B. A.: Ozone Photochemistry in the Antarctic Stratosphere in Summer, Q. J. Roy. Meteor. Soc., 111, 1013–1025, 1985.

The spring 2011 final stratospheric warming above Eureka

C. Adams et al.

Title Page

Abstract | Introduction

Conclusions | References

Tables | Figures

◀◀ | ▶▶

◀ | ▶

Back | Close

Full Screen / Esc

Fayt, C., De Smedt, I., Letocart, V., Merlaud, A., Pinardi, G., and Van Roozendael, M.: QDOAS Software user manual version 1.00: http://uv-vis.aeronomie.be/software/QDOAS/index.php (last access: 15 February 2012), 2011.

Fleischmann, O. C., Hartmann, M., Burrows, J. P., and Orphal, J.: New ultraviolet absorption cross-sections of BrO at atmospheric temperatures measured by time-windowing Fourier transform spectroscopy, J. Photoch. Photobio. A, 168, 117–132, 2004.

Fraser, A., Goutail, F., Strong, K., Bernath, P. F., Boone, C., Daffer, W. H., Drummond, J. R., Dufour, D. G., Kerzenmacher, T. E., Manney, G. L., McElroy, C. T., Midwinter, C., McLinden, C. A., Nichitiu, F., Nowlan, C. R., Walker, J., Walker, K. A., Wu, H., and Zou, J.: Intercomparison of UV-visible measurements of ozone and NO_2 during the Canadian Arctic ACE validation campaigns: 2004–2006, Atmos. Chem. Phys., 8, 1763–1788, doi:10.5194/acp-8-1763-2008, 2008.

Fraser, A., Adams, C., Drummond, J. R., Goutail, F., Manney, G., and Strong, K.: The Polar Environment Atmospheric Research Laboratory UV-visible ground-based spectrometer: first measurements of O_3, NO_2, BrO, and OClO columns, J. Quant. Spectrosc. Ra., 110, 986–1004, doi:10.1016/j.jqsrt.2009.02.034, 2009.

Greenblatt, G. D., Orlando, J. J., Burkholder, J. B., and Ravishankara, A. R.: Absorption-measurements of oxygen between 330 nm and 1140 nm, J. Geophys. Res., 95, 18577–18582, 1990.

Harvey, V. L., Hitchman, M. H., Pierce, R. B., and Fairlie, T. D.: Tropical aerosol in the Aleutian High, J. Geophys. Res., 104, 6281–6290, 1999.

Harvey, V. L., Pierce, R. B., Fairlie, T. D., and Hitchman, M. H.: A climatology of stratospheric polar vortices and anticyclones, J. Geophys. Res., 107, 4442, doi:10.1029/2001JD001471, 2002.

Harvey, V. L., Pierce, R. B., Hitchman, M. H., Randall, C. E., and Fairlie, T. D.: On the distribution of ozone in stratospheric anticyclones, J. Geophys. Res., 109, D24308, doi:10.1029/2004JD004992, 2004.

Harvey, V. L., Randall, C. E., Manney, G. L., and Singleton, C. S.: Low-ozone pockets observed by EOS-MLS, J. Geophys. Res., 113, D17112, doi:10.1029/2007JD009181, 2008.

Hendrick, F., Pommereau, J.-P., Goutail, F., Evans, R. D., Ionov, D., Pazmino, A., Kyrö, E., Held, G., Eriksen, P., Dorokhov, V., Gil, M., and Van Roozendael, M.: NDACC/SAOZ UV-visible total ozone measurements: improved retrieval and comparison with correlative ground-based and

The spring 2011 final stratospheric warming above Eureka

C. Adams et al.

Title Page

Abstract | Introduction

Conclusions | References

Tables | Figures

|◄ | ►|

◄ | ►

Back | Close

Full Screen / Esc

Printer-friendly Version

Interactive Discussion

satellite observations, Atmos. Chem. Phys., 11, 5975–5995, doi:10.5194/acp-11-5975-2011, 2011.

Hess, P. G.: Mixing Processes Following the Final Stratospheric Warming, J. Atmos. Sci., 48, 1625–1641, 1991.

Hood, L. L., Soukharev, B. E., Fromm, M., and McCormack, J. P.: Origin of extreme ozone minima at middle to high northern latitudes, J. Geophys. Res., 106, 20925–20940, 2001.

Iwao, K. and Hirooka, T.: Dynamical quantifications of ozone minihole formation in both hemispheres, J. Geophys. Res., 111, D02104, doi:10.1029/2005JD006333, 2006.

James, P. M.: A climatology of ozone mini-holes over the northern hemisphere, Int. J. Climatol., 18, 1287–1303, 1998.

Kerzenmacher, T. E., Walker, K. A., Strong, K., Berman, R., Bernath, P. F., Boone, C. D., Drummond, J. R., Fast, H., Fraser, A., MacQuarrie, K., Midwinter, C., Sung, K., McElroy, C. T., Mittermeier, R. L., Walker, J., and Wu, H. J.: Measurements of O_3, NO_2 and temperature during the 2004 Canadian Arctic ACE Validation Campaign, Geophys. Res. Lett., 32, L16S07, doi:10.1029/2005GL023032, 2005.

Konopka, P., Engel, A., Funke, B., Mueller, R., Grooss, J.-U., Guenther, G., Wetter, T., Stiller, G., von Clarmann, T., Glatthor, N., Oelhaf, H., Wetzel, G., Lopez-Puertas, M., Pirre, M., Huret, N., and Riese, M.: Ozone loss driven by nitrogen oxides and triggered by stratospheric warmings can outweigh the effect of halogens, J. Geophys. Res., 112, D05105, doi:10.1029/2006JD007064, 2007.

Lahoz, W. A., Geer, A. J., and Orsolini, Y. J.: Northern Hemisphere stratospheric summer from MIPAS observations, Q. J. Roy. Meteor. Soc., 133, 197–211, 2007.

Levelt, P. F., Van den Oord, G. H. J., Dobber, M. R., Malkki, A., Visser, H., de Vries, J., Stammes, P., Lundell, J. O. V., and Saari, H.: The Ozone Monitoring Instrument, IEEE T. Geosci. Remote, 44, 1093–1101, 2006.

Lindenmaier, R., Strong, K., Batchelor, R. L., Chipperfield, M. P., Daffer, W. H., Drummond, J. R., Duck, T. J., Fast, H., Feng, W., Fogal, P. F., Kolonjari, F., Manney, G. L., Manson, A., Meek, C., Mittermeier, R. L., Nott, G. J., Perro, C., and Walker, K. A.: Unusually low ozone, HCl, and HNO_3 column measurements at Eureka, Canada during winter/spring 2011, Atmos. Chem. Phys., 12, 3821–3835, doi:10.5194/acp-12-3821-2012, 2012.

Llewellyn, E., Lloyd, N. D., Degenstein, D. A., Gattinger, R. L., Petelina, S. V., Bourassa, A. E., Wiensz, J. T., Ivanov, E. V., McDade, I. C., Solheim, B. H., McConnell, J. C., Haley, C. S., von Savigny, C., Sioris, C. E., McLinden, C. A., Griffioen, E., Kaminski, J., Evans, W. F. J., Puckrin,

The spring 2011 final stratospheric warming above Eureka

C. Adams et al.

Title Page

Abstract	Introduction
Conclusions	References
Tables	Figures

◄ | ►►

◄ | ►

Back | Close

Full Screen / Esc

Printer-friendly Version

Interactive Discussion

E., Strong, K., Wehrle, V., Hum, R. H., Kendall, D. J. W., Matsushita, J., Murtagh, D. P., Brohede, S., Stegman, J., Witt, G., Barnes, G., Payne, W. F., Piche, L., Smith, K., Warshaw, G., Deslauniers, D. L., Marchand, P., Richardson, E. H., King, R. A., Wevers, I., McCreath, W., Kyrola, E., Oikarinen, L., Leppelmeier, G. W., Auvinen, H., Megie, G., Hauchecorne, A., Lefevre, F., de La Noe, J., Ricaud, P., Frisk, U., Sjoberg, F., von Scheele, F., and Nordh, L.: The OSIRIS instrument on the Odin spacecraft, Can. J. Phys., 82, 411–422, 2004.

Manney, G. L., Zurek, R. W., Oneill, A., and Swinbank, R.: On The Motion of Air Through the Stratospheric Polar Vortex, J. Atmos. Sci., 51, 2973–2994, 1994.

Manney, G. L., Froidevaux, L., Waters, J. W., Zurek, R. W., Gille, J. C., Kumer, J. B., Mergenthaler, J. L., Roche, A. E., Oneill, A., and Swinbank, R.: Formation Of Low-Ozone Pockets In The Middle Stratospheric Anticyclone During Winter, J. Geophys. Res., 100, 13939–13950, 1995a.

Manney, G. L., Zurek, R. W., Froidevaux, L., Waters, J. W., Oneill, A., and Swinbank, R.: Lagrangian Transport Calculations Using UARS Data. 2. Ozone, J. Atmos. Sci., 52, 3069–3081, 1995b.

Manney, G. L., Livesey, N. J., Jimenez, C. J., Pumphrey, H. C., Santee, M. L., MacKenzie, I. A., and Waters, J. W.: EOS Microwave Limb Sounder observations of "frozen-in" anticyclonic air in arctic summer, Geophys. Res. Lett., 33, L06810, doi:10.1029/2005GL025418, 2006.

Manney, G. L., Daffer, W. H., Zawodny, J. M., Bernath, P. F., Hoppel, K. W., Walker, K. A., Knosp, B. W., Boone, C., Remsberg, E. E., Santee, M. L., Harvey, V. L., Pawson, S., Jackson, D. R., Deaver, L., McElroy, C. T., McLinden, C. A., Drummond, J. R., Pumphrey, H. C., Lambert, A., Schwartz, M. J., Froidevaux, L., McLeod, S., Takacs, L. L., Suarez, M. J., Trepte, C. R., Cuddy, D. C., Livesey, N. J., Harwood, R. S., and Waters, J. W.: Solar occultation satellite data and derived meteorological products: Sampling issues and comparisons with Aura Microwave Limb Sounder, J. Geophys. Res., 112, D24S50, doi:10.1029/2007JD008709, 2007.

Manney, G. L., Santee, M. L., Rex, M., Livesey, N. J., Pitts, M. C., Veefkind, P., Nash, E. R., Wohltmann, I., Lehmann, R., Froidevaux, L., Poole, L. R., Schoeberl, M. R., Haffner, D. P., Davies, J., Dorokhov, V., Gernandt, H., Johnson, B., Kivi, R., Kyro, E., Larsen, N., Levelt, P. F., Makshtas, A., McElroy, C. T., Nakajima, H., Parrondo, M. C., Tarasick, D. W., von der Gathen, P., Walker, K. A., and Zinoviev, N. S.: Unprecedented Arctic ozone loss in 2011, Nature, 478, 469–475, doi:10.1038/nature10556, 2011.

The spring 2011 final stratospheric warming above Eureka

C. Adams et al.

Title Page

Abstract | Introduction

Conclusions | References

Tables | Figures

◄ | ►

◄ | ►

Back | Close

Full Screen / Esc

Printer-friendly Version

Interactive Discussion

McPeters, R., Kroon, M., Labow, G., Brinksma, E., Balis, D., Petropavlovskikh, I., Veefkind, J. P., Bhartia, P. K., and Levelt, P. F.: Validation of the Aura Ozone Monitoring Instrument total column ozone product, J. Geophys. Res., 113, D15S14, doi:10.1029/2007JD008802, 2008.

Morris, G. A., Kawa, S. R., Douglass, A. R., Schoeberl, M. R., Froidevaux, L., and Waters, J.: Low-ozone pockets explained, J. Geophys. Res., 103, 3599–3610, 1998.

Murtagh, D., Frisk, U., Merino, F., Ridal, M., Jonsson, A., Stegman, J., Witt, G., Eriksson, P., Jimenez, C., Megie, G., de la Noe, J., Ricaud, P., Baron, P., Pardo, J. R., Hauchcorne, A., Llewellyn, E. J., Degenstein, D. A., Gattinger, R. L., Lloyd, N. D., Evans, W. F. J., McDade, I. C., Haley, C. S., Sioris, C., von Savigny, C., Solheim, B. H., McConnell, J. C., Strong, K., Richardson, E. H., Leppelmeier, G. W., Kyrola, E., Auvinen, H., and Oikarinen, L.: An overview of the Odin atmospheric mission, Can. J. Phys., 80, 309–319, 2002.

Nair, H., Allen, M., Froidevaux, L., and Zurek, R. W.: Localized rapid ozone loss in the northern winter stratosphere: An analysis of UARS observations, J. Geophys. Res., 103, 1555–1571, 1998.

Orsolini, Y. J., Eskes, H., Hansen, G., Hoppe, U. P., Kylling, A., Kyro, E., Notholt, J., Van Der A, R., and Von Der Gathen, P.: Summertime low-ozone episodes at northern high latitudes, Q. J. Roy. Meteor. Soc., 129, 3265–3275, 2003.

Orsolini, Y. J. and Nikulin, G.: A low-ozone episode during the European heatwave of August 2003, Q. J. Roy. Meteor. Soc., 132, 667–680, 2006.

OSIRIS: Odin-OSIRIS NO_2 data product: http://osirus.usask.ca/?q_node/245 (last access: 30 November 2010), 2011.

Perliski, L. M., Solomon, S., and London, J.: On the Interpretation of Seasonal-Variations of Stratospheric Ozone, Planet. Space Sci., 37, 1527–1538, 1989.

Peters, D., Egger, J., and Entzian, G.: Dynamical Aspects of Ozone Mini-Hole Formation, Meteorol. Atmos. Phys., 55, 205–214, 1995.

Ravishankara, A. R., Daniel, J. S., and Portmann, R. W.: Nitrous Oxide (N_2O): The Dominant Ozone-Depleting Substance Emitted in the 21st Century, Science, 326, 123–125, 2009.

Reinecker, M. M.: The GEOS-5 data assimilation system - Documentation of versions 5.0.1, and 5.2.0, NASA Tech. Memo., TM-2008-104606, 27, 97, 2008.

Rienecker, M. M., Suarez, M. J., Gelaro, R., Todling, R., Bacmeister, J., Liu, E., Bosilovich, M. G., Schubert, S. D., Takacs, L., Kim, G.-K., Bloom, S., Chen, J., Collins, D., Conaty, A., da Silva, A., Gu, W., Joiner, J., Koster, R. D., Lucchesi, R., Molod, A., Owens, T., Pawson, S., Pegion, P., Redder, C. R., Reichle, R., Robertson, F. R., Ruddick, A. G., Sienkiewicz,

Title Page

Abstract | Introduction

Conclusions | References

Tables | Figures

|◄ | ►|

◄ | ►

Back | Close

Full Screen / Esc

Printer-friendly Version

Interactive Discussion

M., and Woollen, J.: MERRA: NASA's Modern-Era Retrospective Analysis for Research and Applications, J. Climate, 24, 3624–3628, 2011.

Rothman, L. S., Barbe, A., Benner, D. C., Brown, L. R., Camy-Peyret, C., Carleer, M. R., Chance, K., Clerbaux, C., Dana, V., Devi, V. M., Fayt, A., Flaud, J. M., Gamache, R. R., Goldman, A., Jacquemart, D., Jucks, K. W., Lafferty, W. J., Mandin, J. Y., Massie, S. T., Nemtchinov, V., Newnham, D. A., Perrin, A., Rinsland, C. P., Schroeder, J., Smith, K. M., Smith, M. A. H., Tang, K., Toth, R. A., Vander Auwera, J., Varanasi, P., and Yoshino, K.: The HITRAN molecular spectroscopic database: edition of 2000 including updates through 2001, J. Quant. Spectrosc. Ra., 82, 5–44, doi:10.1016/S0022-4073(03)00146-8, 2003.

Ruth, S. L., Remedios, J. J., Lawrence, B. N., and Taylor, F. W.: Measurements of N_2O by the UARS Improved Stratospheric and Mesospheric Sounder during the Early Northern Winter 1991/92, J. Atmos. Sci., 51, 2818–2833, 1994.

Sander, S. P., Friedl, R. R., Barker, J. R., Golden, D. M., Kurylo, M. J., Wine, P. H., Abbatt, J., Brukholder, J. B., Kolb, C. E., Moortgat, G. K., Huie, R. E., and Orkin, V. L.: Chemical Kinetics and Photochemical Data for Use in Atmospheric Studies Evaluation Number 17, JPL Publication 10-6, Jet Propulsion Laboratory, California Institude of Technology, Pasadena, California, 1–684, 2011.

Sinnhuber, B. M., Muller, R., Langer, J., Bovensmann, H., Eyring, V., Klein, U., Trentmann, J., Burrows, J. P., and Kunzi, K. F.: Interpretation of mid-stratospheric Arctic ozone measurements using a photochemical box-model, J. Atmos. Chem., 34, 281–290, 1999.

Strahan, S. E., Duncan, B. N., and Hoor, P.: Observationally derived transport diagnostics for the lowermost stratosphere and their application to the GMI chemistry and transport model, Atmos. Chem. Phys., 7, 2435–2445, doi:10.5194/acp-7-2435-2007, 2007.

Thieblemont, R., Huret, N., Orsolini, Y. J., Hauchecorne, A., and Drouin, M. A.: Frozen-in anticyclones occurring in polar Northern Hemisphere during springtime: Characterization, occurrence and link with quasi-biennial oscillation, J. Geophys. Res., 116, D20110, doi:10.1029/2011JD016042, 2011.

Vandaele, A. C., Hermans, C., Simon, P. C., Carleer, M., Colin, R., Fally, S., Merienne, M. F., Jenouvrier, A., and Coquart, B.: Measurements of the NO_2 absorption cross-section from 42 000 cm^{-1} to 10 000 cm^{-1} (238-1000 nm) at 220 K and 294 K, J. Quant. Spectrosc. Ra., 59, 171–184, 1998.

Veefkind, P., and Sneep, M.: OMDOA03 README FILE: http://disc.sci.gsfc.nasa.gov/Aura/data-holdings/OMI/documents/v003/OMDOAO3_README_V003.shtml (last access: 14 January 2012), 2009.

Veefkind, J. P., de Haan, J. R., Brinksma, E. J., Kroon, M., and Levelt, P. F.: Total ozone from the Ozone Monitoring Instrument (OMI) using the DOAS technique, IEEE T. Geosci. Remote, 44, 1239–1244, 2006.

Wahner, A., Tyndall, G. S., and Ravishankara, A. R.: Absorption cross-sections for OClO as a function of temperature in the wavelength range 240–480 nm, J. Phys. Chem., 91, 2734–2738, 1987.

WMO: Scientific Assessment of Ozone Depletion: 2002, Rep. 50, Global Ozone Research and Monitoring Project, World Meteorological Society, Geneva, Switzerland, 2003.

WMO: Scientific Assessment of Ozone Depletion: 2010, Rep. 52, Global Ozone Research and Monitoring Project, World Meteorological Society, Geneva, Switzerland, 2011.

Wohltmann, I. and Rex, M.: The Lagrangian chemistry and transport model ATLAS: validation of advective transport and mixing, Geosci. Model Dev., 2, 153–173, doi:10.5194/gmd-2-153-2009, 2009.

Wohltmann, I., Lehmann, R., and Rex, M.: The Lagrangian chemistry and transport model ATLAS: simulation and validation of stratospheric chemistry and ozone loss in the winter 1999/2000, Geosci. Model Dev., 3, 585–601, doi:10.5194/gmd-3-585-2010, 2010.

Title Page

Abstract | Introduction

Conclusions | References

Tables | Figures

◄ | ►

◄ | ►

Back | Close

Full Screen / Esc

Printer-friendly Version

Interactive Discussion
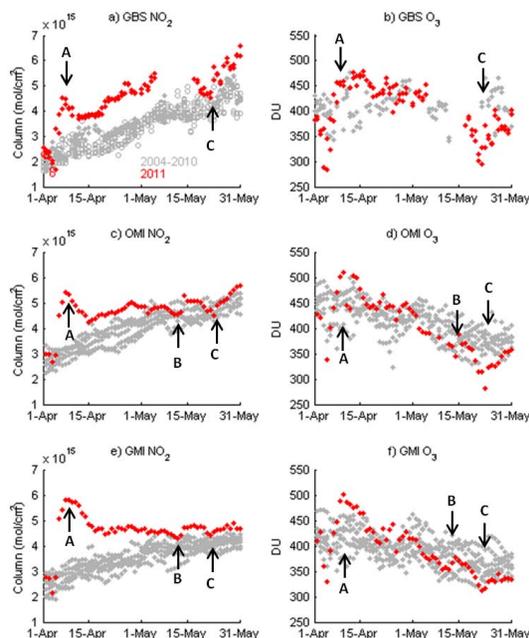
Fig. 1. Timeseries of NO_2 and ozone columns above Eureka for 1 April to 31 May in 2011 (red) and in 2004–2011 (grey). **(a)** GBS-vis (closed circles) and GBS-UV (open circles) NO_2 partial columns (17 km to top of atmosphere) and **(b)** GBS ozone total columns, both measured both in morning and evening twilights. **(c)** OMI stratospheric NO_2 columns and **(d)** OMI total ozone columns averaged daily within 500 km of Eureka. **(e)** NO_2 and **(f)** ozone total columns from daily GMI output from 10:00–10:30 a.m. local time at Eureka. Note that there are fewer ozone than NO_2 GBS measurements because, for some years, spring-time dedicated BrO measurements excluded the visible wavelengths used to measure ozone. Black arrows labelled A, B, C indicate 8 April, 13 May, and 22 May, respectively.

The spring 2011 final stratospheric warming above Eureka

C. Adams et al.
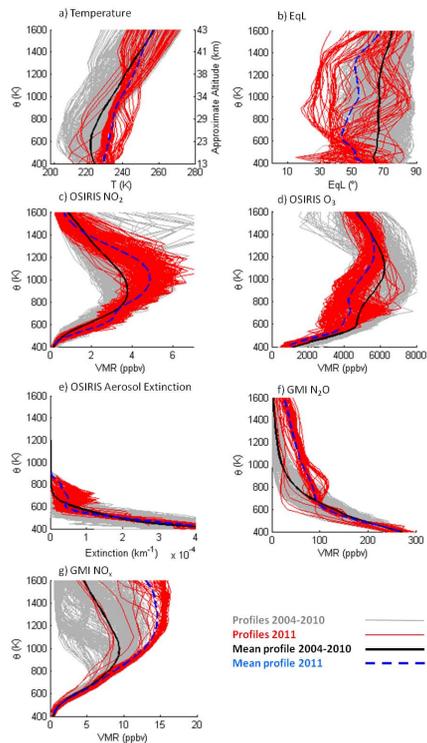
Fig. 2. Profiles of meteorological fields and composition above PEARL for 1 April to 31 May. Thin grey and thick black lines indicate individual profiles and average profiles, respectively for 2004–2010. Thin red lines and thick blue dashed lines indicate individual profiles and average profiles, respectively for 2011. **(a)** Temperature and **(b)** EqL from GEOS-5 DMPs at 12:00 UTC above Eureka. **(c)** NO_2, **(d)** ozone, and **(e)** aerosol extinction from OSIRIS measurements within 500 km of Eureka. **(f)** N_2O and **(g)** NO_x from GMI daily profiles above Eureka. The approximate altitude corresponding to the potential temperature levels is shown in the y-axis of **(a)**. VMRs are given in parts per billion by volume (ppbv).
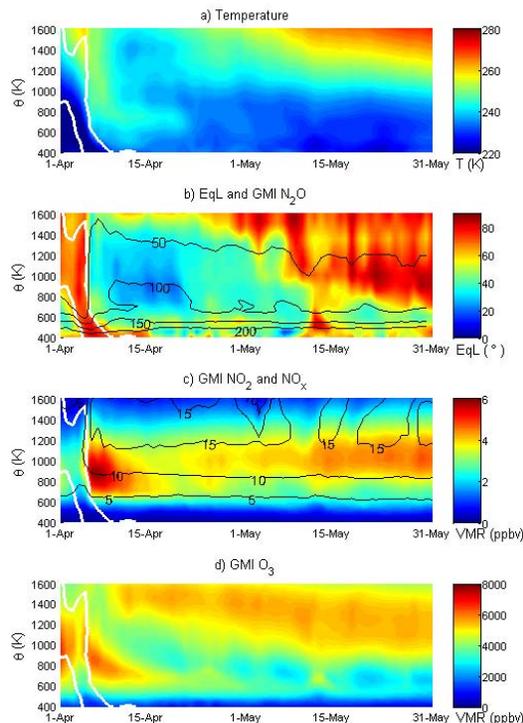
Fig. 3. Time-potential temperature plots above Eureka for April/May 2011. **(a)** Temperature from GEOS-5 DMPs. **(b)** EqL (color-scale) from GEOS-5 DMPs and N_2O (black contour lines, with labels given in ppbv) from GMI. **(c)** NO_2 (color-scale) and NO_x (black contour lines, with labels given in ppbv) from GMI. **(d)** Ozone from GMI. Low [high] temperatures, EqLs, and VMRs are given in blue [red]. Thick white lines indicate boundaries of the polar vortex determined by sPV $= 1.6 \times 10^{-4}$ s^{-1}.
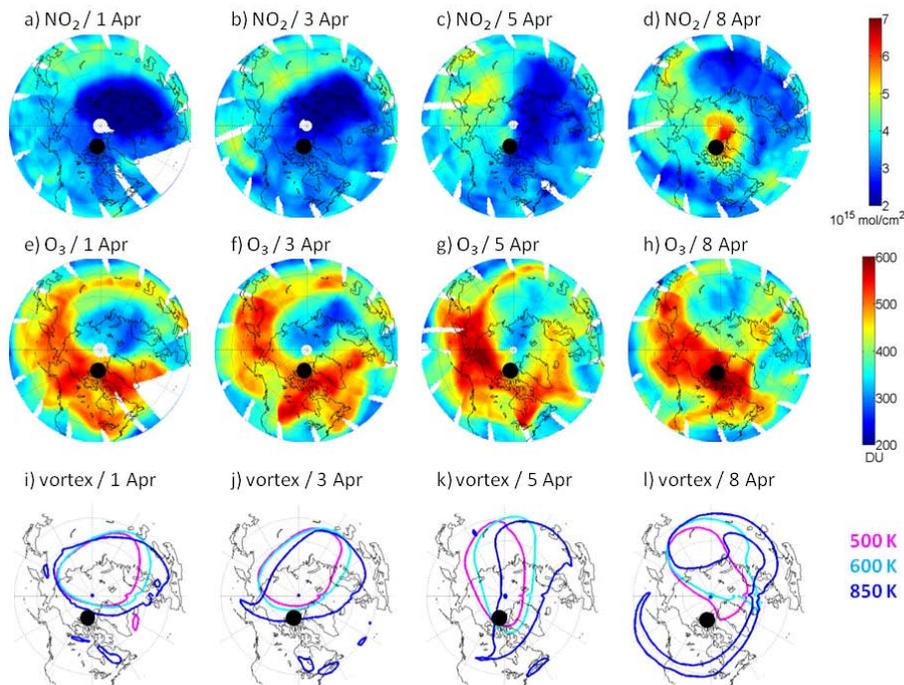
Fig. 4. Polar maps of OMI NO_2 stratospheric columns (top row), OMI ozone total columns (middle row) and the approximate inner vortex edge (bottom row) for 1, 3, 5 and 8 April 2011. Small [large] column values are given in blue [red]. The inner vortex edge is approximated at sPV = 1.6×10^{-4} s^{-1} for 500-K (magenta), 600-K (cyan), and 850-K (blue) potential temperature levels. Eureka is indicated by the black circle.
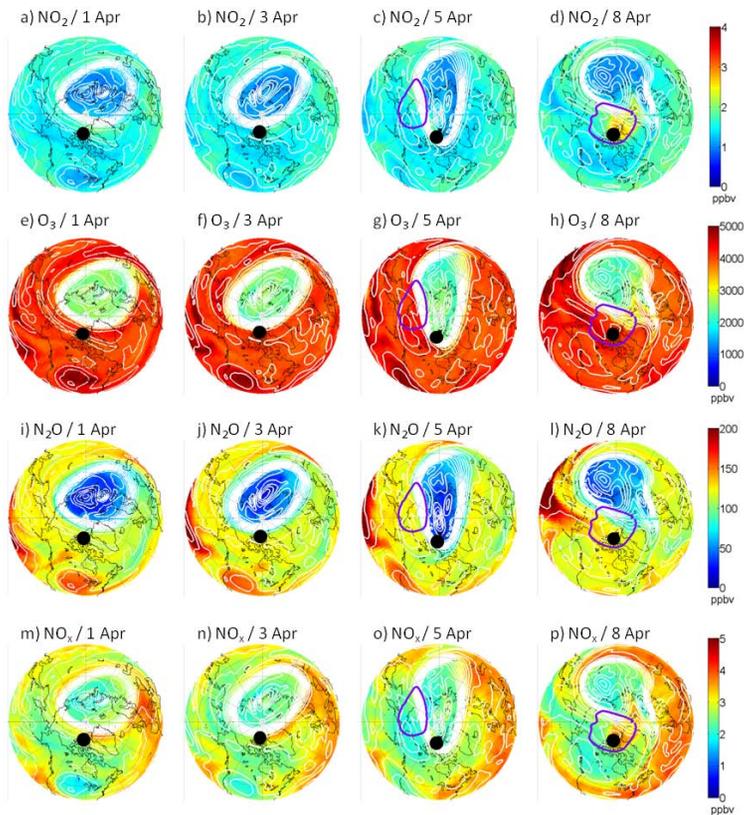
Fig. 5. Polar maps at the 600-K (∼ 23-km) potential temperature level of GMI NO_2 (top row), ozone (top middle row), N_2O (bottom middle row), and NO_x (bottom row) VMRs for 1, 3, 5 and 8 April 2011. Low [high] VMRs are given in blue [red]. White lines indicate PV contours. The area enclosed by the purple contour indicates $T > 235$ K. Eureka is indicated by the black circle.
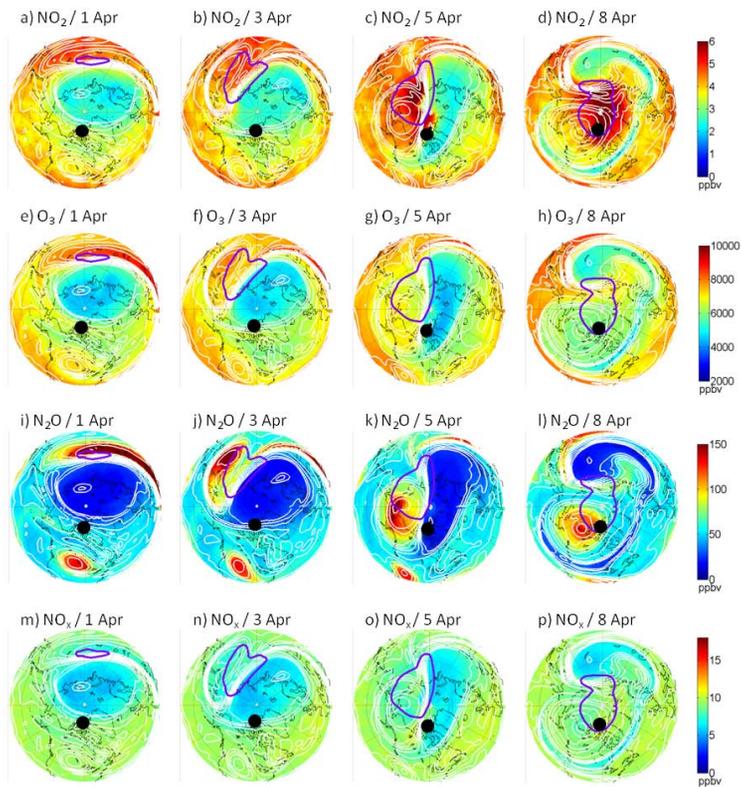
Fig. 6. As for Fig. 5 at the 850-K ($\sim$ 31-km) potential temperature level. The area enclosed by the purple contour indicates $T > 245$ K. Note that color scales are different from Fig. 5.

Full Screen / Esc

Printer-friendly Version

Interactive Discussion
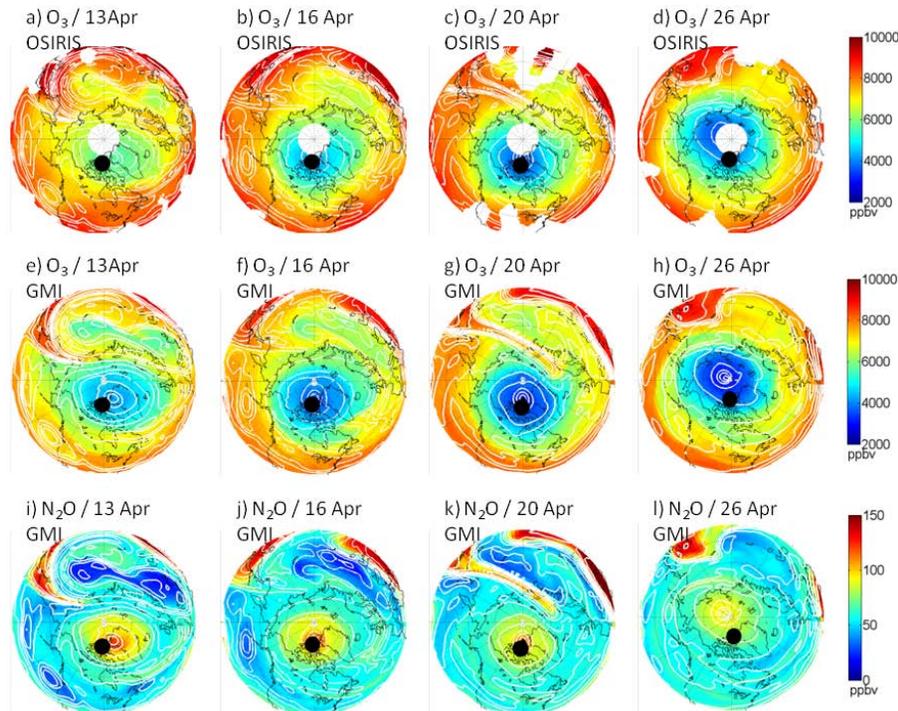
Fig. 7. Polar maps at the 850-K potential temperature level of OSIRIS ozone (top row), GMI ozone (middle row), and GMI N$_2$O (bottom row) VMRs for 13, 16, 20, 26 April 2011. Low [high] VMRs are given in blue [red]. White lines indicate PV contours. Eureka is indicated by the black circle.

The spring 2011 final stratospheric warming above Eureka

C. Adams et al.

Title Page

Abstract | Introduction

Conclusions | References

Tables | Figures

◀ | ▶|

◀ | ▶

Back | Close

Full Screen / Esc

Printer-friendly Version

Interactive Discussion

a) Ozone VMRs at 600 K
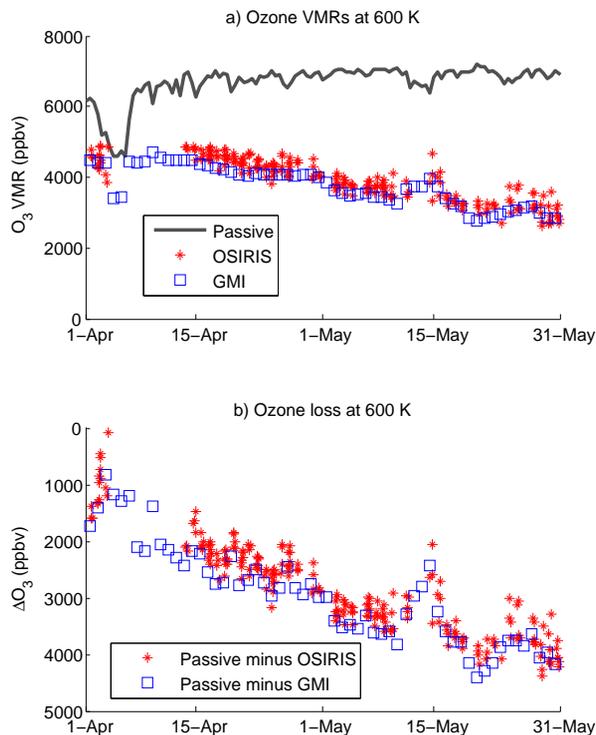
b) Ozone loss at 600 K

Fig. 8. (a) 2011 ozone VMRs at the 600-K potential temperature level from ATLAS passive ozone above Eureka (black line), OSIRIS ozone measurements within 500 km of Eureka (red stars), and GMI ozone above Eureka (blue squares). **(b)** Ozone loss calculated for ATLAS passive ozone minus OSIRIS (red stars) and ATLAS passive ozone minus GMI (blue squares). The black arrow labelled B indicates 13 May.

ACPD

12, 20033–20072, 2012

The spring 2011 final stratospheric warming above Eureka

C. Adams et al.

Title Page

Abstract | Introduction

Conclusions | References

Tables | Figures

◄ | ►

◄ | ►

Back | Close

Full Screen / Esc

Printer-friendly Version

Interactive Discussion
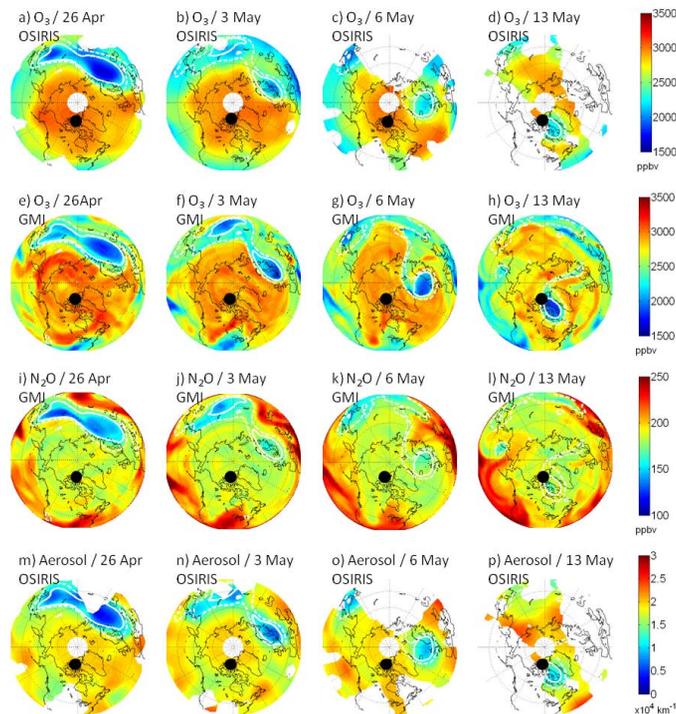
Fig. 9. Polar maps at the 500-K (∼ 18 km) potential temperature level of ozone VMR (top row), GMI ozone VMR (top middle row), GMI N_2O VMR (bottom middle row), and OSIRIS aerosol extinction at 750 nm (bottom row) for 26 April and 3, 6, 13 May 2011. Low [high] VMRs and aerosol extinctions are given in blue [red]. The white dashed lines indicate sPV = 1.2×10^{-4} s^{-1} (the approximate outer vortex edge) and the thick white lines indicate sPV = 1.6×10^{-4} s^{-1} (the approximate inner vortex edge). Eureka is indicated by the black circle.

Fig. 10. Formation of ozone mini-hole above Eureka: **(a)** OMI ozone total columns, **(b)** GMI tropopause pressure, **(c)** GMI ozone VMR at 400 K ($\sim$ 13 km), and **(d)** GMI N_2O VMR at 400 K. For ozone and N_2O, low [high] VMRs are given in blue [red]. The color scale for the tropopause pressure is reversed so that low pressures (high altitudes) are in red and high pressures (low altitudes) are in blue. The white contour lines indicate the geopotential height, with thick lines indicating 13.4 and 13.6 km and thin dashed lines indicating > 13.6 km on 0.2-km intervals. Eureka is indicated by the black circle.